

## EXPERIMENTAL AND NUMERICAL INVESTIGATION OF PREMIXED TUBULAR FLAMES

DAVID M. MOSBACHER,<sup>1</sup> JOSEPH A. WEHRMEYER,<sup>1</sup> ROBERT W. PITZ,<sup>1</sup> CHIH-JEN SUNG<sup>2</sup>  
AND JOHN L. BYRD<sup>3</sup>

<sup>1</sup>*Mechanical Engineering Department  
Vanderbilt University  
Box 1592 Station B  
Nashville, TN 37235, USA*

<sup>2</sup>*Mechanical and Aerospace Engineering Department  
Case Western Reserve University  
Cleveland, OH 44106, USA*

<sup>3</sup>*Engineering Technology Department  
Austin Peay State University  
Clarksville, TN 37044, USA*

Fundamental flame response in a stretched and curved flow field is investigated in a unique optically accessible tubular burner. Time-averaged, one-dimensional spatially resolved temperature and major species measurements are obtained in a set of stretched,  $\phi = 0.175$  premixed  $\text{H}_2/\text{air}$  tubular flames using visible laser-induced Raman spectroscopy. The very lean  $\text{H}_2/\text{air}$  flames are formed under relatively high stretch rates,  $90 \leq \kappa \leq 215 \text{ s}^{-1}$ , with  $227 \text{ s}^{-1}$  being the extinction condition. In tubular flames, both stretch and thermal-diffusive effects are dependent on both aerodynamic straining and flame curvature. Thermal-diffusive effects in highly curved ( $\sim 2 \text{ mm}$  flame radius) tubular flames significantly influence the flame structure, leading to flame temperature increases of  $\sim 120 \text{ K}$  over the planar unstretched flame temperature ( $\sim 1180 \text{ K}$ ). The standard program for modeling stretched planar flames (Oppdif) is modified for the cylindrical geometry of the tubular flame. Comparisons of the Raman measurements with numerical simulations for tubular premixed flames, using complex chemistry and detailed transport properties, show excellent agreement at low rates of stretch (i.e.,  $\kappa \leq 127 \text{ s}^{-1}$ ). At higher flame stretch, hence increased curvature, numerical simulations using the currently available transport data and chemical kinetic mechanisms incorrectly predict the flame structure. The experimental observations show extinction occurring ( $\sim 227 \text{ s}^{-1}$ ), while numerical simulations overpredict the extinction limit ( $\sim 750 \text{ s}^{-1}$ ). Simulations using four different  $\text{H}_2/\text{air}$  chemical kinetic mechanisms show that the flame structure is very sensitive to the particular mechanism and the molecular diffusion coefficients. Evaluation of molecular diffusion coefficients indicates that the thermodiffusive properties of the deficient reactant species,  $\text{H}_2$ , strongly affect the tubular flame structure. Thus, the products in the flame zone ( $\phi = 0.34$ ) are enriched from the initial reactant mixture ( $\phi = 0.175$ ) by flame curvature and the rapid diffusion of  $\text{H}_2$ .

### Introduction

Flame-flow interaction is a fundamental problem of interest in combustion research. Experimentally, burners using a variety of flow fields have been used to study flame behavior: for example, Bunsen flames [1], counterflow stagnation flames [2], slot-burner flames [3,4], and so on. In these burners, the effects of both stretch and curvature on flame behavior have been investigated. Theoretically, the effects of curvature and stretch have been examined under turbulent [5,6] and laminar conditions [7–9]. However, quantitatively evaluating the effects of stretch and curvature in these flames has proved difficult because typically the stretch rates and degree of curvature are small and vary across the flame front.

Most of the quantitative work on flame-flow interaction has concentrated on stretched premixed laminar planar flames produced between two counterflowing coaxial jets (opposed jets) [10,11]. In this flow configuration, the flow field only interacts with the one-dimensional flame sheet through aerodynamic straining.

In this work, a unique optically accessible counterflow stagnation burner with cylindrical geometry produces curved (tubular) flames under high rates of stretch. The tubular flame is a geometrical conversion of the twin counterflow flame: that is, it is a stretched flame, but its cross-sectional shape is cylindrical [12]. Tubular flames exhibit the same stretch effects observed in planar flames, but with amplification due to curvature. Thus, stretch and

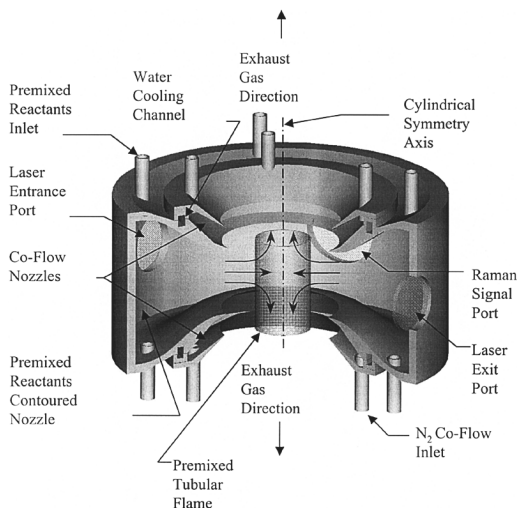


FIG. 1. Schematic of radial counterflow tubular burner design.

thermodiffusive effects are related to the degree of curvature and aerodynamic straining of the tubular flame. If  $Le \neq 1$  (where  $Le$ , the Lewis number, equals thermal diffusivity,  $\alpha$ , over the mass diffusivity,  $D$ ) for the incoming reactant mixture, the local flame temperature responds according to the coupled effects of aerodynamic straining, flame curvature, and  $Le$  [6–9,12]. The changes in flame structure depend upon whether the flame curvature is concave or convex to the incoming reacting mixture. A premixed flame sheet can possess a local temperature above or below the adiabatic flame temperature because of the “focusing” or “defocusing,” due to curvature, of both heat release and the molecular diffusion of the deficient reactant.

Premixed tubular flames have been previously examined both experimentally and numerically. Using a rotating flow burner similar to Ishizuka [13], Yamamoto et al. [14] experimentally investigated tubular premixed flames created in a low stretch vortex. Ishizuka [15] and Ogawa et al. [16] injected premixed reactants radially inward through the walls of an open porous cylindrical tube to examine curvature effects at low rates of stretch. Using a burner that directed premixed reactants radially inward around the flame circumference, Kobayashi and Kitano [17] examined the extinction characteristics of propane/air and methane/air premixed tubular flames at high rates of stretch and compared them to similar opposed jet flames. Tubular premixed flames have been analyzed numerically in order to predict flame structure and extinction as functions of the inlet velocity boundary condition [18–21]. In these previous studies, the experimental measurements in the tubular flames were limited as the burners had minimal optical access.

## Tubular Burner

The tubular burner, as shown in Fig. 1, is similar to that of Ref. [17]. A premixed combustible mixture is introduced to the outer circular chamber (stagnation chamber) via a plenum (not shown) with 16 circumferentially spaced inlet ports. In the stagnation chamber, the reactant mixture diffuses through fine-gauge (00) stainless steel wool, which is used to provide a uniform radial pressure drop. The mixture exits the burner through a converging cylindrical nozzle of 1.5 cm radius and 2 cm height, that forces the flow toward the axial centerline. A premixed tubular flame, with products exiting radially inward from the flame and the reactants flowing radially inward toward the flame, is formed around the cylindrical axis of the burner. The flame location is the radial position where the burning velocity balances with the upstream radial velocity of the unburned mixture. In this manner, premixed tubular flames of various radii can be formed by adjusting the reactant mixture velocity, thus controlling the degree of curvature and aerodynamic straining.

The axisymmetric flow field in the tubular burner, as described in Refs. [7,8,12–21], radially converges and axially diverges. Consequently, the tubular flame is stabilized by a finite rate of stretch. The influence of aerodynamic straining and curvature on flame stretch is determined by evaluating an invariant expression for stretch in a stationary flame [22]. A specific expression for the global stretch rate,  $\kappa$ , in the tubular flame can be derived from this expression and is given as

$$\kappa \cong \frac{2\mathbf{V}}{R} \quad (1)$$

where  $\mathbf{V}$  is the radial inlet velocity and  $R$  is the nozzle radius (1.5 cm).

A unique feature of the tubular burner is the provision of three optical access ports (Fig. 1). Two laser access ports, located at  $180^\circ$  from each other, are 25 mm in diameter. A third, 50 mm diameter optical port, located at right angles to the laser ports, is used by the light detection system to collect scattered light. Additionally, coflow nitrogen ports, located around the nozzle exits, stabilize the tubular flame by shielding it from the ambient air and significantly reducing the amount of combustion outside the burner. Water-cooling jackets, located around the top and bottom of the tubular burner, prevent preheating of the reactant mixture. The axis of symmetry of the burner and its flame is vertically oriented.

## Experimental System

A schematic of the experimental system is shown in Fig. 2. Visible laser Raman spectroscopy is used

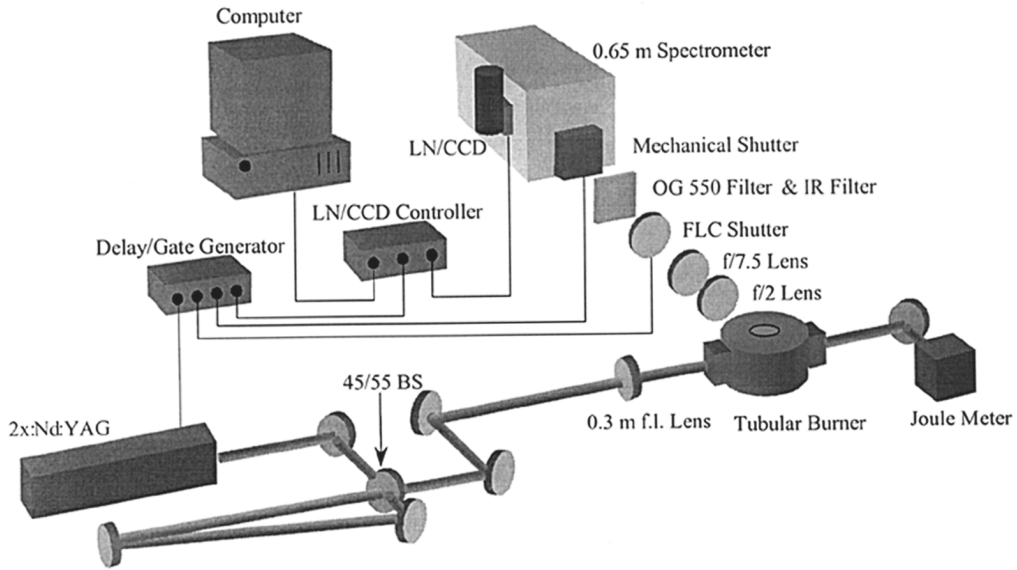


FIG. 2. Schematic diagram of the visible Raman setup.

to measure temperature and species concentrations through the flame. The Raman signals are created by a frequency-doubled, pulsed (10 Hz) Nd:YAG (532 nm) laser. The laser output is focused to a beam waist of  $\sim 0.25$  mm to improve spatial resolution transverse to the laser beam. Energy output of the laser is limited to  $\sim 225$  mJ/pulse due to losses from a mirrors-beamsplitter arrangement, which is used to prevent laser-induced breakdown at the laser focus by stretching the effective pulse length from 7 to  $\sim 35$  ns.

The Raman scattered light is collected at  $90^\circ$  to the laser beam using a 75 mm diameter  $f/2$  achromat and relayed by another lens into a modified single-grating spectrograph [23]. The light detector is a cryogenically cooled, back-illuminated CCD array ( $1024 \times 1024$  pixels), allowing one-dimensional spatially resolved time-averaged measurements of Raman signals from all major species. The measured spatial resolution of the imaging system is  $\sim 120 \mu\text{m}$  along the 4.6 mm imaged length of the laser.

A 2.5 mm thick OG-550 colored-glass filter and an IR filter are mounted in series at the entrance slit to minimize the amount of 532 nm and stray IR light entering the spectrograph. To efficiently gate the camera and reduce time-continuous background flame luminosity, a  $44 \mu\text{s}$  ferroelectric liquid crystal shutter is used in series with a 6 ms mechanical shutter at the spectrometer entrance slit, with both open only during the laser pulse. A total of 600 single-pulse Raman images are averaged on the CCD. For the Raman measurements, the laser beam passes through the diameter of the flame tube at the zero axial position (the axial plane of the stagnation

point). Based on the spatial resolution of the system, each integrated line-wise image provides  $\sim 38$  useable measurement points. Given the sampling length of the imaging system, the burner is translated once in the zero axial plane, thus allowing the flame structure along the entire diameter of the flame tube to be recorded. Fig. 3 shows a set of Raman spectra obtained in a tubular flame.

The experimental measurements are derived from the Raman signals through an experimental calibration of the Raman system, using several calibration flames produced in a "Hencken" multielement flat-flame diffusion burner. The ideal gas law is used to relate measured total number density to temperature assuming atmospheric pressure. For calibration conditions, fuel- and air-flow rates were measured with mass flow meters with accuracies of  $\pm 1\%$  of their full scale. The accuracy of the temperature measurements,  $\pm 2.5\%$ , was evaluated by comparing experimental Raman temperature measurements from  $\text{H}_2/\text{air}$  calibration flames with adiabatic flame temperatures based on measured reactant flow rates.

### Numerical Simulations

In order to numerically model premixed tubular flames, the standard Oppdif [24] program was modified to account for the radial geometry. Oppdif normally models opposed jet flames of axial symmetry, where the reactants originate along the symmetry axis and exit radially away from the axis. Flame structure is then mapped onto the axial dimension. In a tubular flame, the radial coordinate, instead of the

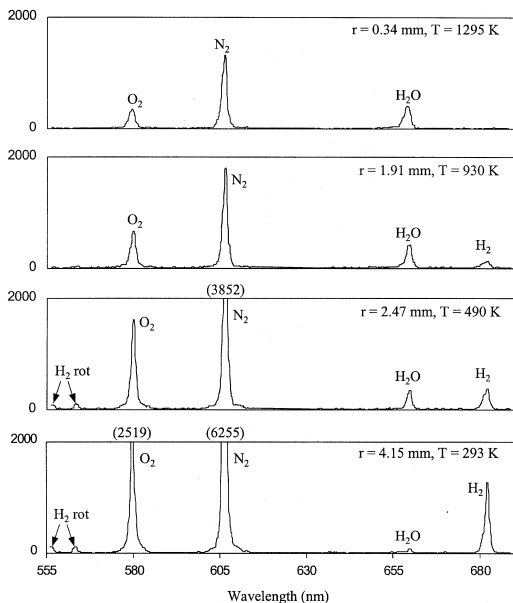


FIG. 3. Time-averaged, background subtracted spectra from line-imaged Raman scattering in a laminar, premixed  $\text{H}_2/\text{air}$  tubular flame ( $\phi = 0.175$ ,  $\kappa = 104 \text{ s}^{-1}$ ). Spectra correspond to four radial positions from the stagnation centerline of the flame: burned gas, initial reaction, preheat, and unburned gas regions. Some peaks are cut off for clarity, and their peak values are given in parenthesis.

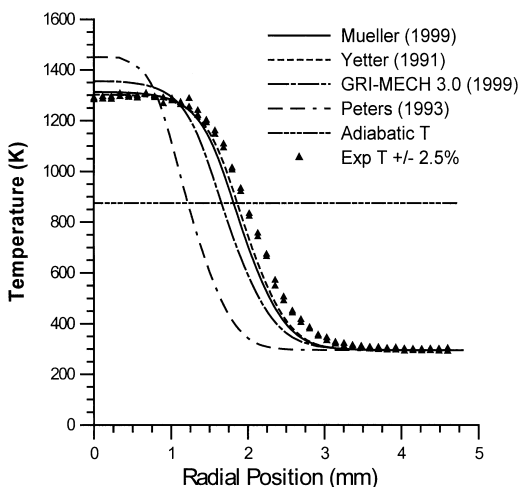


FIG. 4. Comparison of predicted temperature profiles from four reaction mechanisms in a premixed  $\text{H}_2/\text{air}$  tubular flame ( $\phi = 0.175$ ,  $\kappa = 90 \text{ s}^{-1}$ ).

axial coordinate, is used as the spatial dimension through which flame structure is mapped. By transforming the spatial coordinate and seeking a similarity solution of the two-dimensional conservation equations, the tubular flame can be modeled as a two-point boundary value problem. The Oppdif program was modified for the tubular flame geometry, and the resulting set of differential equations for the tubular flame are given in Ref. [20].

Numerical simulations for the experimental premixed  $\text{H}_2/\text{air}$  tubular flames examined were performed with detailed transport and complex chemistry. Molecular transport properties were determined from mixture-averaged calculations using Chapman-Enskog collision theory, Lennard-Jones potentials, and reference data from the CHEMKIN [24] transport database. The model includes thermal diffusion for light species (molecular weights  $\leq 4$ ). Multicomponent calculations were found to give marginal improvement in accuracy and consequently were not used due to increased computation time.  $\text{H}_2/\text{O}_2$  chemical kinetic mechanisms from Mueller et al. [25], Yetter et al. [26], Peters [27], and the relevant  $\text{H}_2/\text{O}_2$  reactions in GRI-MECH 3.0 [28] were used to investigate flame structure response to chemistry, with these mechanisms using 19, 19, 17, and 25 reversible elementary reactions, respectively, all with nine chemical species. Thermochemical properties were determined from the CHEMKIN thermodynamic database, except for recommendations provided in the chemistry mechanisms. Gas-phase radiation in the optically thin limit was assumed, using the Planck mean absorption coefficients obtained from Refs. [29,30].

## Results and Discussion

To investigate the effects of curvature at various degrees of stretch ( $90 \text{ s}^{-1} \leq \kappa \leq 215 \text{ s}^{-1}$ ), a set of lean premixed  $\text{H}_2/\text{air}$  tubular flames ( $Le < 1$ ) at  $\phi = 0.175$  were measured. Fig. 4 shows a comparison of Raman temperature measurements with numerical simulations using the four different chemical kinetic reaction mechanisms [25–28] including thermal diffusion for light species. Data from both sides of the tubular flame centerline are plotted versus radius to illustrate the axisymmetric structure of the flame. The adiabatic equilibrium flame temperature is also shown by the horizontal line at  $\sim 875 \text{ K}$  to emphasize thermal-diffusion/curvature effects. Fig. 4 is for a flame with a stretch rate of  $90 \text{ s}^{-1}$  and measured temperature of  $\sim 1295 \text{ K}$ , which is  $\sim 420 \text{ K}$  above the adiabatic flame temperature of the reactant mixture ( $\phi = 0.175$ ). Comparison of the mechanisms reveals that the kinetics of Mueller et al. and Yetter et al. are the strongest, leading to higher flame speeds, larger flame radii, less fuel focusing, and lower flame temperatures. Reaction mechanism trends illustrated in Fig. 4 are representative of all

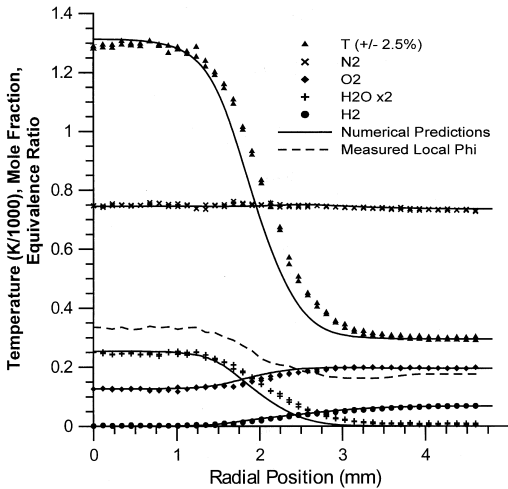


FIG. 5. Raman-derived and numerically predicted product measurements using Mueller et al. chemistry with thermal diffusion in a  $\phi = 0.175$ ,  $\kappa = 90 \text{ s}^{-1}$   $\text{H}_2/\text{air}$  tubular flame.

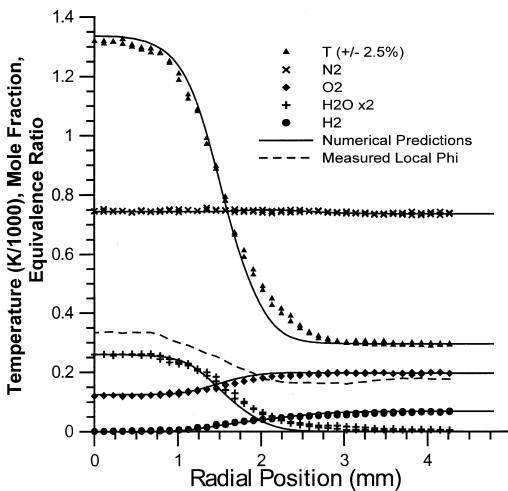


FIG. 6. Raman-derived and numerically predicted product measurements using Mueller et al. chemistry with thermal diffusion in a  $\phi = 0.175$ ,  $\kappa = 127 \text{ s}^{-1}$   $\text{H}_2/\text{air}$  tubular flame.

the stretch rates examined. The Mueller et al. and Yetter et al. mechanisms predict similar trends; however, the Mueller et al. mechanism, which uses more recently reported reaction rate data, is used in the remainder of the numerical simulations. The predicted flame radius,  $\sim 2.1 \text{ mm}$ , and temperature,  $\sim 1310 \text{ K}$ , using the Mueller et al. chemistry (with inclusion of thermal diffusion for light species) are in good agreement with the Raman measurements. Only slight differences are seen between prediction

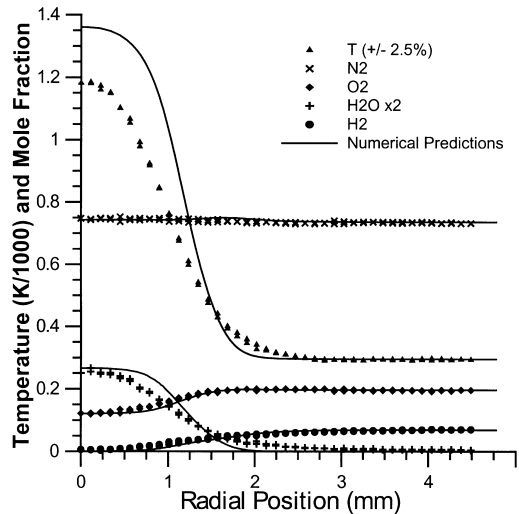


FIG. 7. Raman-derived and numerically predicted product measurements using Mueller et al. chemistry with thermal diffusion in a  $\phi = 0.175$ ,  $\kappa = 190 \text{ s}^{-1}$   $\text{H}_2/\text{air}$  tubular flame.

and measurement. The predicted flame radius is slightly smaller and measured temperatures show a slight decrease near the flame centerline, possibly due to radiation heat loss. However, numerical simulations that include radiation heat loss predict a negligible loss in temperature of  $\sim 2 \text{ K}$ , due to the lean operating condition.

Figs. 5–7 show comparisons of Raman temperature and species concentrations measurements for tubular flames of  $\kappa = 90, 127$ , and  $190 \text{ s}^{-1}$ , respectively. Numerical simulations using the Mueller et al. chemistry mechanism with inclusion of thermal diffusion show good agreement for  $\text{H}_2$ ,  $\text{N}_2$ ,  $\text{H}_2\text{O}$ , and  $\text{O}_2$  profiles in Figs. 5 and 6. Convolution of the data from spatial averaging is minimal because of the relatively “thick” flames studied herein, and hence the spatial resolution used to analyze the spectra,  $120 \mu\text{m}$ , adequately resolves the flame.

At higher stretch rates ( $\kappa > 127 \text{ s}^{-1}$ , seen in Fig. 7), incomplete reaction occurs in the experiments as indicated by the reduced flame temperature ( $\sim 1185 \text{ K}$ ) and  $\text{H}_2\text{O}$  mole fraction. The numerical predictions are not in agreement with the experiments and overpredict the temperature by  $\sim 180 \text{ K}$ . Use of other chemical mechanisms [26–28] does not improve the comparison. Thus, improvements to the chemical kinetic mechanisms are needed to more accurately model lean-limit highly stretched tubular flames.

The effects of thermal diffusion for light species for a  $\kappa = 90$  and  $190 \text{ s}^{-1}$  tubular flame are shown in Figs. 8 and 9, respectively. If the thermal diffusion correction is not included in the simulation for the  $\kappa = 90 \text{ s}^{-1}$  flame, the flame temperature ( $\sim 1285 \text{ K}$ )

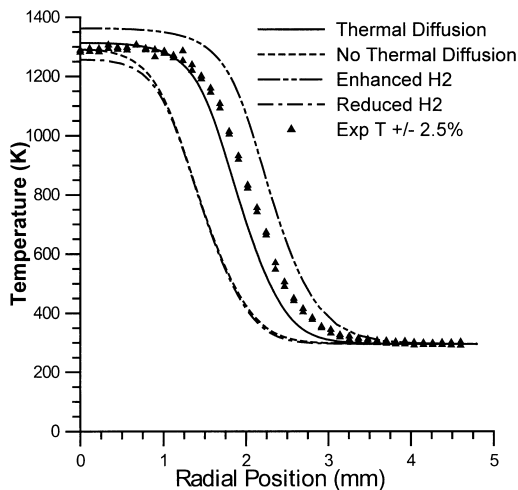


FIG. 8. Simulation using Mueller et al. chemistry showing effects of thermal diffusion coefficient and increasing/decreasing the binary diffusion coefficient of  $H_2$  into  $N_2$  by  $+32\%/ -29\%$  in a  $H_2$ /air tubular flame ( $\phi = 0.175$ ,  $\kappa = 90 \text{ s}^{-1}$ ).

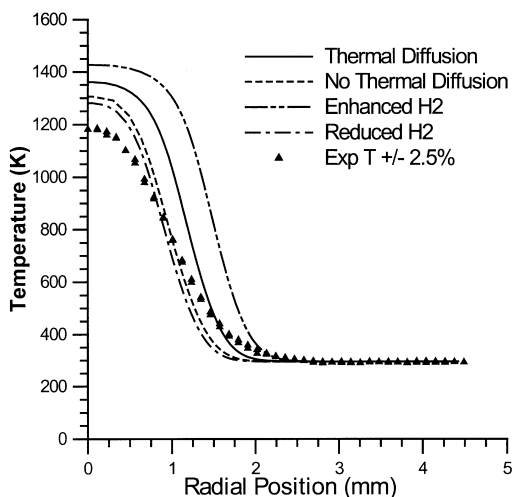


FIG. 9. Simulation using Mueller et al. chemistry showing effects of thermal diffusion coefficient and increasing/decreasing the binary diffusion coefficient of  $H_2$  into  $N_2$  by  $+32\%/ -29\%$  in a  $H_2$ /air tubular flame ( $\phi = 0.175$ ,  $\kappa = 190 \text{ s}^{-1}$ ).

and radius ( $\sim 1.5 \text{ mm}$ ) are underpredicted. However, as illustrated in Fig. 9, incomplete reaction occurs at higher stretch rates (as indicated in Fig. 7) and the numerical simulations with and without inclusion of the thermal diffusion correction grossly overpredict flame temperature and radius. The results in Figs. 8 and 9 suggest that the increased mass

flux of  $H_2$ , or light species, with increasing temperature due to thermal diffusion and diffusive focusing is important in high temperature gradients characteristic of curved flames.

Figures 8 and 9 also show the importance of diffusive focusing of  $H_2$  in the tubular flame. The binary diffusion coefficient for  $H_2$  was increased/decreased by decreasing/increasing by  $\sqrt{2}$  the Lennard-Jones collision diameter. When the binary diffusion coefficient of  $H_2$  into  $N_2$  is increased/decreased  $+32\%/ -29\%$ , the flame temperature changes  $+50\%/ -60 \text{ K}$  and  $+66\%/ -79 \text{ K}$  and the flame radius changes by  $+18\%/ -22\%$  and  $+22\%/ -23\%$  for the  $\kappa = 90$  and  $190 \text{ s}^{-1}$  flames, respectively. Due to the focusing effect from curvature, enhancing the diffusion of  $H_2$  causes the flame to become a richer, stronger flame, while the opposite occurs for reducing  $H_2$  diffusion. Additionally, enhancing or reducing  $H_2$ ,  $H_2O$ , and  $OH$  diffusion has minimal effect on the premixed tubular flame structure, that is,  $\sim \pm 3 \text{ K}$  and no change in flame radius. The effect of rapid  $H_2$  diffusion can be seen in Figs. 5 and 6 where the reactants initially at  $\phi = 0.175$  ( $T_{\text{adiabatic}} = 875 \text{ K}$ ) are enriched such that the products in the flame are at  $\phi = 0.34$  ( $T_{\text{adiabatic}} \cong 1305 \text{ K} \cong$  measured  $T_{\text{postflame zone}} \cong 1300 \text{ K}$ ). Thus, the postflame gases are in adiabatic equilibrium in the enriched mixture.

The thermal-diffusive effects in Figs. 8 and 9 illustrate the sensitivity of the tubular flame to the transport data. Further improvements in the numerical simulations can be made by implementing more current transport packages as they become available. Paul [31] demonstrated the inaccuracies of the current CHEMKIN package by comparing predicted transport properties as functions of temperature with experimental data. Furthermore, replacing the stiff  $1/r^{12}$  repulsive term in the Lennard-Jones potential with an exponential repulsive term can improve the accuracy of the calculated transport properties of species with low molecular weights over a broader range of temperature,  $50\text{--}2200 \text{ K}$  [31].

The coupled effect of stretch and curvature in tubular flames is shown in Fig. 10 by plotting the variations in numerically predicted and measured flame temperatures and radii versus stretch. Flame radius is taken as the distance from the stagnation centerline of the flame to the half-maximum of the temperature profile. Examination of Fig. 10 reveals that  $H_2$ /air tubular flames of  $\phi = 0.175$  decrease in radius from  $\sim 2.25$  to  $1.05 \text{ mm}$  as stretch is increased, and extinction occurs at  $\sim 227 \text{ s}^{-1}$  when the thermal flame thickness becomes on the order of the flame radius. At low stretch rates (decreased curvature), for  $\kappa \leq 127 \text{ s}^{-1}$ , the flame freely adjusts to the flow conditions, resulting in large flame radius and minor flame temperature responses. However, at increased stretch rates (increased curvature), for  $\kappa > 127 \text{ s}^{-1}$ , the increased aerodynamic straining pins the tubular flame near the stagnation centerline, dissipating heat

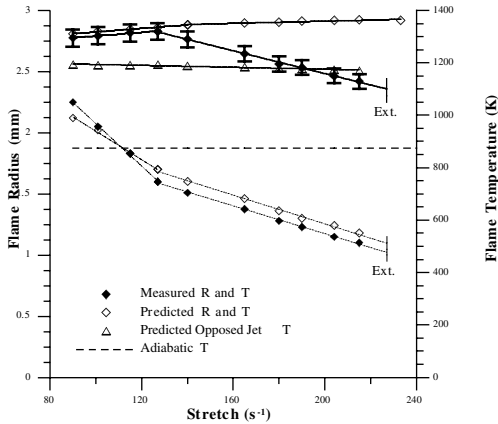


FIG. 10. Comparison of flame radius and peak flame temperature versus stretch for  $H_2$ /air tubular flames of  $\phi = 0.175$ . Numerical simulations of opposed jet flames under identical conditions are shown for comparison.

and driving extinction [6,9,12,17]. The numerical simulations accurately predict this curvature/aerodynamic straining transition for flame radius but not for flame temperature. At high rates of stretch,  $\kappa > 127 \text{ s}^{-1}$ , numerical simulations do not correctly predict when extinction occurs. The numerical extinction limit for the tubular flame is  $\sim 750 \text{ s}^{-1}$ . Additionally, examining the measured and predicted thermal flame thickness in Figs. 8 and 9 and extinction characteristics in Fig. 10 indicate that transport errors are minor compared to uncertainties in flame chemistry. In investigations of flame/stretch interactions in premixed spherical flames, similar discrepancies between experimental measurements and numerical simulations have been reported [32,33].

The influence of curvature on thermal-diffusive effects is also shown in Fig. 10 by comparing the tubular flame results with numerical predictions of opposed jet planar flames. Simulations of the opposed jet flames, using the tubular flame boundary velocities and a nozzle separation distance of  $2R$  (thus keeping the stretch rates the same between the planar and tubular flame cases), were made with Oppdif. The adiabatic equilibrium flame temperature is also shown for reference. Numerical simulations of the opposed jet flame indicate that flame structure is relatively insensitive to aerodynamic straining, due to the propagation nature of the premixed flame [9]. For opposed jet planar flames from  $\kappa = 10$  to  $90 \text{ s}^{-1}$ , the flame temperature increases  $\sim 30 \text{ K}$  followed by a  $\sim 30 \text{ K}$  decrease from  $\kappa = 90$  to  $215 \text{ s}^{-1}$ . In the low stretch limit,  $\kappa \leq 127 \text{ s}^{-1}$ , curvature-enhanced thermal-diffusive effects in the tubular flame increase the flame temperature  $\sim 10\%$  ( $120 \text{ K}$ ) over the unstretched planar flame,  $\sim 1180 \text{ K}$ . As  $\kappa$  decreases, the tubular flame approaches the

planar limit and curvature effects diminish, thus indicating that, for  $Le \leq 1$  mixtures, the tubular flame is stronger than the opposed jet flame due to flame curvature [17,34]. Additionally, the inherent thermal-diffusive effects in premixed flames of  $Le \leq 1$  mixtures are illustrated in Fig. 10 by comparing the tubular and opposed jet planar flame results with the adiabatic flame temperature of the reactant mixture ( $\phi = 0.175$ ).

## Conclusions

A unique optically accessible tubular burner has been developed that allows the use of non-intrusive laser diagnostics. Using visible Raman scattering, complete major species concentrations and temperature profiles have been measured in a set of highly stretched lean limit premixed hydrogen/air tubular flames. The premixed hydrogen/air tubular flames formed in this burner have flame temperatures that are  $\sim 120 \text{ K}$  (10%) above the planar unstretched flame temperature ( $1180 \text{ K}$ ) due to curvature enhanced thermal-diffusive effects. Sensitivity of the flame structure to the chemical kinetic mechanism and molecular transport data has been demonstrated by comparing the Raman-derived measurements with numerical simulations. Comparisons of measured temperature and major species concentrations profiles with numerical simulations are in good agreement for flames of low stretch ( $\kappa \leq 127 \text{ s}^{-1}$ ). At these conditions, the molecular transport data and chemical kinetic mechanism are capable of predicting the structure of the  $H_2$ /air tubular flame. Rapid diffusion of the deficient reactant species,  $H_2$ , is shown to be significant in determining the structural characteristics of the tubular flame, while the diffusion of other radical species (e.g.,  $H$ ,  $H_2O$ ,  $OH$ ) exhibit little influence. Diffusion of  $H_2$  results in an initial reactant mixture ( $\phi = 0.175$ ) that is enriched in the postflame gases that are in equilibrium at the enriched fuel/air ratio ( $\phi = 0.34$ ). However, at higher flame stretch, hence increased curvature, the numerical simulations using the currently available transport data and chemistry mechanisms overpredict flame temperature and flame radius. As discussed, the inability of the numerical simulations to correctly predict flame structure in lean premixed highly stretched and curved  $H_2$ /air flames, where thermal-diffusive effects are dominant, suggests that a more detailed investigation of the low and intermediate temperature chemistry and transport data and the validity of the self-similarity model assumption for small radii is warranted.

## Acknowledgments

The authors would like to acknowledge Drs. M. Smooke and F. Dryer for their insightful discussions and the U.S.

Department of Energy's Office of Basic Energy Sciences who have supported this work through a Partnership for Academic-Industrial Research, PAIR, grant (no. DE-FG02-98ER14915, with Dr. Alan H. Laufer as technical monitor).

## REFERENCES

- Law, C. K., Ishizuka, S., and Cho, P., *Combust. Sci. Technol.* 28:89 (1982).
- Barlow, R. S., Karpetis, A. N., Frank, J. H., and Chen, J. Y., *Combust. Flame* 127:2102 (2001).
- Choi, C. W., and Puri, I. K., *Combust. Flame* 126:164 (2001).
- Echekki, T., and Mungal, M. G., *Proc. Combust. Inst.* 23:455 (1990).
- Echekki, E., and Chen, J. H., *Combust. Flame* 106:184 (1996).
- Poinsot, T., Veynante, D., and Candel, S., *J. Fluid Mech.* 228:561 (1991).
- Buckmaster, J. D., and Crowley, A. B., *J. Fluid Mech.* 131:341 (1983).
- Mikolaitis, D. W., *Combust. Flame* 57:25 and 58:23 (1984).
- Law, C. K., and Sung, C. J., *Prog. Energy Combust. Sci.* 26:459 (2000).
- Tanoff, M. A., Smooke, M. D., Osborne, R. J., Brown, T. M., and Pitz, R. W., *Proc. Combust. Inst.* 26:1121 (1996).
- Sung, C. J., Liu, J. B., and Law, C. K., *Combust. Flame* 106:168 (1996).
- Ishizuka, S., *Prog. Energy Combust. Sci.* 19:187 (1993).
- Ishizuka, S., *Combust. Flame* 75:367 (1989).
- Yamamoto, K., Ishizuka, S., and Hirano, T., *Proc. Combust. Inst.* 25:1399 (1994).
- Ishizuka, S., *Proc. Combust. Inst.* 20:287 (1984).
- Ogawa, Y., Saito, N., and Liao, C., *Proc. Combust. Inst.* 27:3221 (1998).
- Kobayashi, H., and Kitano, M., *Combust. Flame* 76:285 (1989).
- Nishioka, M., Inagaki, K., Ishizuka, S., and Takeno, T., *Combust. Flame* 86:90 (1991).
- Libby, P., Peters, N., and Williams, F., *Combust. Flame* 75:265 (1989).
- Smooke, M. D., and Giovangigli, V., *Proc. Combust. Inst.* 23:447 (1990).
- Ju, Y., Matsumi, H., Takita, K., and Masuya, G., *Combust. Flame* 116:580 (1999).
- Matalon, M., *Combust. Sci. Technol.* 31:169 (1983).
- Osborne, R. J., Wehrmeyer, J. A., and Pitz, R. W., AIAA paper 2000-0776.
- Kee, R. J., Rupley, F., Miller, J., Coltrin, M., Grear, J., Meeks, E., Moffat, H., Lutz, A., Dixon-Lewis, G., Smooke, M., Warnatz, J., Evans, G., Larson, R., Mitchell, R., Petzold, L., Reynolds, L., Caracotsios, M., Stewart, W., and Glarborg, P., *User Manual, The CHEMKIN Collection Release 3.5*, Reaction Design, Inc., San Diego, CA, 1999.
- Mueller, M. A., Kim, T. J., Yetter, R. A., and Dryer, F., *Int. J. Chem. Kinet.* 31:113 (1999).
- Yetter, R. A., Dryer, F. L., and Rabitz, H., *Combust. Sci. Technol.* 79:97 (1991).
- Peters, N., in *Reduced Kinetic Mechanisms for Applications in Combustion Systems* (N. Peters and B. Rogg, eds.), Springer-Verlag, Berlin, 1993, Chapters 1, 5.
- Smith, G. P., Golden, D. M., Frenklach, M., Moriarty, N. W., Eiteneer, B., Goldenberg, M., Bowman, C. T., Hanson, R. K., Song, S., Gardiner, W. C., Lissianski, V. V., and Qin, Z., GRI-Mech homepage, Gas Research Institute, Chicago, 1999, [www.me.berkeley.edu/gri\\_mech/](http://www.me.berkeley.edu/gri_mech/).
- Rothman, L. S., Gamachee, R. R., Tipping, R. H., Rinsland, C. P., Smith, M. A. H., Benner, D. C., Devi, V. M., Flaud, J. M., Peyret, C. C., Perrin, A., Goldman, A., Massie, S. T., Brown, L. R., and Toth, R. A., *J. Quant. Spectrosc. Radiat. Trans.* 48:469 (1992).
- Soufiani, A., and Taine, J., *Int. J. Heat Mass Transfer* 40:987 (1997).
- Paul, P. H., *DRFM: A New Package for the Evaluation of Gas-Phase-Transport Properties*, Sandia report SAND98-8203.
- Kwon, O. C., and Faeth, G. M., *Combust. Flame* 124:590 (2001).
- Wu, M. S., Ronney, P. D., Colantonio, R. O., and Vanzandt, D. M., *Combust. Flame* 116:387 (1999).
- Kobayashi, H., and Kitano, M., *Combust. Sci. Technol.* 75:227 (1991).